



# Efficient evolution of reactive oxygen species over the coordinated $\pi$ -delocalization $g\text{-C}_3\text{N}_4$ with favorable charge transfer for sustainable pollutant elimination



Jingjie Liu<sup>a,1</sup>, Chuanbao Xiong<sup>a,b,1</sup>, Shujuan Jiang<sup>a,b,\*</sup>, Xi Wu<sup>a,b</sup>, Shaoqing Song<sup>a,b,\*</sup>

<sup>a</sup> Laboratory of Atmospheric Environment, Key Laboratory of Nuclear Resources and Environment (State), East China University of Technology, 418 Guanglan Road, Nanchang 330013, PR China

<sup>b</sup> School of Materials Science and Chemical Engineering, Ningbo University, 818 Fenghua Road, Ningbo 315211, PR China

## ARTICLE INFO

### Keywords:

$g\text{-C}_3\text{N}_4$   
 $\pi$ -Delocalization structure  
Charge transfer  
Photocatalysis  
Reactive oxygen species

## ABSTRACT

Reactive oxygen species (ROS) as efficient and green oxidants can be generated through various catalytic methods, which is important for environmental chemistry and chemical engineering. Here we construct an efficient photocatalytic system to evolve ROS for environmental purification. In the work, the coordinated  $g\text{-C}_3\text{N}_4$  photocatalysts ( $\text{Cu}/\text{C}_3\text{N}_4$ ) are designed by interacting N 2p lone electrons at vacancy site of tri-s-triazine polymer with 3d orbits of  $\text{Cu}^{2+}$ , resulting in the extended  $\pi$ -delocalization structure of  $g\text{-C}_3\text{N}_4$ . Experimental and theoretical calculations confirm that the extended  $\pi$ -delocalization structure of  $\text{Cu}/\text{C}_3\text{N}_4$  strengthens the light capturing capability from ultraviolet to near infrared light, favors the charge transfer from N 2p of  $\text{C}_3\text{N}$  to the linked C, and Cu atoms. As a result, the efficient evolution of ROS including  $\text{O}_2^-$  ( $13 \mu\text{mol L}^{-1} \text{h}^{-1}$ ), and  $\text{H}_2\text{O}_2$  ( $550 \mu\text{mol L}^{-1} \text{h}^{-1}$ ) can be completed over  $\text{Cu}/\text{C}_3\text{N}_4$  photocatalysts.  $\text{Cu}/\text{C}_3\text{N}_4$  photocatalysts results in a highly efficient generation of ROS and also exhibited a sustainable removal efficiency for NO<sub>x</sub> and HCHO, which demonstrates a promising application in the field of environmental purification.

## 1. Introduction

Reactive oxygen species (ROS), such as  $\cdot\text{O}_2^-$ ,  $\cdot\text{OH}$ , and  $\text{H}_2\text{O}_2$ , as highly efficient and green oxidants, are of great importance for environmental chemistry and chemical engineering [1,2]. Currently, these reactive oxygen species can be photocatalytically yielded by  $\text{O}_2$  activation over semiconductor-based photocatalysts under irradiation [3,4]. In the photocatalytic procedure, photo-excited electron ( $e^-$ ) activates and reduces  $\text{O}_2$  into  $\cdot\text{O}_2^-$ , and hole ( $h^+$ ) oxidizes  $\text{H}_2\text{O}$  into  $\cdot\text{OH}$  and/or  $\text{O}_2$  [5,6]. With the in-depth study of photocatalysis theory, numerous types of semiconductor-based photocatalysts, e.g.,  $\text{Ag}_3\text{PO}_4@\text{CoFe}_2\text{O}_4$  [7],  $\text{TiO}_2/\text{C-Dots}$  [8],  $\text{CuO-SiO}_2$  [9],  $\text{AgVO}_3/\text{MoS}_2$  [10],  $\text{AgBiO}_3$  [11], and  $\text{Ag}_3\text{PO}_4$  [12] have been utilized to photocatalytically activate  $\text{O}_2$  for yielding oxygen active species. Thermodynamically, it is relatively difficult for one-electron reduction of  $\text{O}_2$  to  $\cdot\text{O}_2^-$  ( $-0.33 \text{ V}$ ) compared with multi-electron reduction ( $+0.69 \text{ V}$  for  $\text{O}_2/\text{H}_2\text{O}_2$ , and  $+1.23 \text{ V}$  for  $\text{O}_2/\text{H}_2\text{O}$ , respectively) [13]. Kinetically, the photocatalytic reactions between photon-generated carriers and

reactants require several microseconds, however,  $e^-$  recombines  $h^+$  from several picoseconds to dozens of nanoseconds [14], resulting in quenching and thus restricting  $\text{O}_2$  activation [15,16]. Therefore,  $\text{O}_2$  chemical adsorption, and efficient e- transfer illustrates a crucial role in the photocatalytic activation and reduction of  $\text{O}_2$  [17].

$g\text{-C}_3\text{N}_4$ , the  $\pi$ -delocalization tri-s-triazine polymeric compound made up of C and N, has been confirmed to be a visible-light-excited photocatalyst [18–20], and its conduction band potential is  $-1.23 \text{ V}$  versus NHE ( $\text{pH} = 7$ ) [21–23], which is much lower in comparison with potentials of  $\text{O}_2/\cdot\text{O}_2^-$  ( $-0.33 \text{ V}$ ),  $\text{O}_2/\text{H}_2\text{O}_2$  ( $+0.69 \text{ V}$ ), and  $\text{O}_2/\text{H}_2\text{O}$  ( $+1.23 \text{ V}$ ). As a result,  $g\text{-C}_3\text{N}_4$  can usually be used to photocatalytically evolve active oxygen species [24–30]. For instance, Wang et al. constructed the black phosphorus (BP)/ $g\text{-C}_3\text{N}_4$  heterostructure photocatalyst for  $\text{O}_2$  activation and reduction [13]. The heterostructure strengthens visible-light absorption, facilitates charge transfer, and increases the efficiency for the evolution of  $\cdot\text{O}_2^-$  and  $\text{H}_2\text{O}_2$ ; We designed solid-solution-like  $\text{o-C}_3\text{N}_4/\text{Ag}_2\text{SO}_4$  photocatalyst as an efficient photocatalytic system for synthesizing  $\cdot\text{O}_2^-$ ,  $\cdot\text{OH}$ , and  $\text{H}_2\text{O}_2$  [6]. Dong and

\* Corresponding authors at: Laboratory of Atmospheric Environment, Key Laboratory of Nuclear Resources and Environment (State), East China University of Technology, 418 Guanglan Road, Nanchang 330013, PR China.

E-mail addresses: [jiangshujuan@nbu.edu.cn](mailto:jiangshujuan@nbu.edu.cn) (S. Jiang), [songshaoqing@nbu.edu.cn](mailto:songshaoqing@nbu.edu.cn) (S. Song).

<sup>1</sup> These authors contributed equally.

Wang et al. reported that  $\text{H}_2\text{O}_2$  evolution efficiency was promoted over Z-scheme  $g\text{-C}_3\text{N}_4$ /perylene imides [31]. Moreover, the photocatalytic rate for  $\text{H}_2\text{O}_2$  evolution was distinctly enhanced over  $g\text{-C}_3\text{N}_4$  with  $\text{SiW}_{11}$  as cocatalysts [32]. Nevertheless, photocatalytic efficiency over  $g\text{-C}_3\text{N}_4$  always suffers from two shortcomings. One is the existence of vacancy structure in the tri-s-triazine polymer, and the other is the large electronegativity difference between C and N [33–35]. The former directly leads to increase the recombination probability of  $e^-$  and  $h^+$ , and the latter induces the existence of abundant hydrogen bonding in the  $\pi$ -conjugated tri-s-triazine polymer [36,37]. The hydrogen bonding promotes the superposition of the polymer nanosheets, thus hindering the transfer of  $e^-$  within the layers of the delocalized tri-s-triazine nanosheets [36]. Orbit theory calculation reveals isolated electron of N p<sub>z</sub> orbital at vacancy sites. In accordance with the coordination field theory, N lone electron may coordinate vacant p and/or d orbital of metal with the aid of static coulomb effect [6], resulting in patching the vacancy structure of  $g\text{-C}_3\text{N}_4$  and thus extending  $\pi$ -conjugated system. The so-constructed  $g\text{-C}_3\text{N}_4$  with the extended  $\pi$ -conjugated structure will optimize efficient electron transfer. Coordination between metal ion and N induces the charge redistribution of  $g\text{-C}_3\text{N}_4$ , which can improve the electronegativity difference between C and N. Moreover, lone electrons of  $\text{O}_2$  will bond with d orbital of metal, and electrons from d orbital of metal will fill into anti-bonding  $\pi^*$  of  $\text{O}_2$ , which facilitates  $\text{O}_2$  adsorption and activation.

Accordingly, we report an extended  $\pi$ -conjugated  $g\text{-C}_3\text{N}_4$  synthesized by coordinating between  $\text{Cu}^{2+}$  3d orbit and N 2p<sub>z</sub> of tri-s-triazine polymer for efficient evolution of ROS. Experimental and DFT results confirm that charge of  $g\text{-C}_3\text{N}_4$  is redistributed and optimized, reflecting as the slight electronegativity difference between C and N, and charge distribution uniformity because of Cu coordination. The extended  $\pi$ -delocalization tri-s-triazine polymer favors adsorption and activation of  $\text{O}_2$  and  $\text{H}_2\text{O}$ . Besides, the strengthened light absorption from UV to visible and even near infrared, and the optimized electron migration are achieved on the extended  $\pi$ -conjugated  $g\text{-C}_3\text{N}_4$ . The extended  $\pi$ -conjugated  $g\text{-C}_3\text{N}_4$  photocatalyst shows high performance for producing  $\cdot\text{O}_2^-$  and  $\text{H}_2\text{O}_2$  species, which supplies ideas for designing active photocatalysts toward solar energy conversion and environmental purification.

## 2. Experimental

### 2.1. Synthesis of the extended $\pi$ -conjugated $g\text{-C}_3\text{N}_4$ samples

The extended  $\pi$ -conjugated  $g\text{-C}_3\text{N}_4$  samples were synthesized by thermally polymerizing the homogeneous mixture of carbamide and  $\text{Cu}_2(\text{CH}_3\text{COO})_4$ . In the procedure, 10 g carbamide was dissolved into  $\text{Cu}_2(\text{CH}_3\text{COO})_4$  solution (25 mL, 2 mM) and magnetically stirred for 180 min. The homogeneous mixture solution was subsequently heated and stirred at 60 °C until sticky-like sample was formed. The sticky-like sample was placed in muffle furnace, and the sample was thermally polymerized at 540 °C with rate of 5 °C min<sup>-1</sup> for 120 min. After natural cooling, the extended  $\pi$ -conjugated  $g\text{-C}_3\text{N}_4$  sample was obtained and labeled as  $\text{Cu}/\text{C}_3\text{N}_4\text{-1}$ . In order to probe the universality of the method,  $\text{Cu}/\text{C}_3\text{N}_4\text{-2}$  (25 mL, 4 mM), and  $\text{Cu}/\text{C}_3\text{N}_4\text{-3}$  (25 mL, 6 mM) samples were synthesized with using the method of  $\text{Cu}/\text{C}_3\text{N}_4\text{-1}$ , respectively. In the meantime,  $g\text{-C}_3\text{N}_4$  was directly synthesized by thermally polymerizing carbamide at 540 °C for 120 min.

### 2.2. Characterization

Component, crystal structure and chemical valences were tested with using X ray diffraction spectroscopy (Bruker, D8 advance), X ray photo-electron energy spectrum (ESCALAB250xi, Thermo Scientific), and IR Affinity-1 FTIR spectrometer (Shimadzu, Japan). Pattern was surveyed by field-emission-scanning-electron microscope (Hitachi), and transmission-electron microscopy (JEM-2010HR). Cu content was

detected with ICP-AES method on a Perkin-Elmer Optima 4300DV instrument. Brunauer-Emmett-Teller (BET) specific surface area was examined with using  $\text{N}_2$  adsorption-desorption method on a Micromeritics ASAP 2020 instrument. Mott-Schottky data, electrochemical-impedance spectra and transient photo-current signals were achieved on electrochemical-workstation (660C Chenhua Instruments) with using  $\text{Na}_2\text{SO}_4$  and  $\text{KNO}_3$  as electrolyte solutions. Electron-paramagnetic resonances were achieved on MEX-nano, Bruker. Surface photovoltage spectra were detected by changing the potential barriers of the electrode surface in the light or dark on the home-built apparatus. Time-resolved-photo-luminescence spectrum was completed on FLS920 fluorescence-lifetime spectrophotometer (Edinburgh).

### 2.3. DFT calculations

DFT calculations were performed by utilizing Gaussian 09 suite of computational programs. The hybrid-density-functional B3LYP was carried out. Geometry was optimized by 6-31G(d) basis sets on the nonmetal atoms and LANL2DZ effective core-potential on Cu. Mulliken-charge distributions of geometry were achieved at the level of B3LYP/[6-31G(d) + LANL2DZ].

### 2.4. Yield of ROS

ROS were detected with using EPR method. In the procedure, 10 mg  $\text{Cu}/\text{C}_3\text{N}_4$  sample was dispersed into DMPO solution ((3.85% volume ratio, 1.04 mL including 1 mL  $\text{CH}_3\text{OH}$ ). After sample was illuminated for 2 min with using xenon lamp (350 W), and  $\text{DMPO}\cdot\text{O}_2^-$  was examined with EPR instrument. When  $\text{H}_2\text{O}$  was replaced with  $\text{CH}_3\text{OH}$ ,  $\text{DMPO}\cdot\text{OH}$  signals were detected. Photocatalytic yield of  $\cdot\text{O}_2^-$  was calculated by nitroblue-tetrazolium absorbance intensity (NBT) at 260 nm. In the light of 1:4 (molar ratio), yield amount of  $\cdot\text{O}_2^-$  was determined.

$\text{H}_2\text{O}_2$  evolution over  $\text{Cu}/\text{C}_3\text{N}_4$  was also studied. 60 mg sample was dispersed into Schlenk flask (9.1% volume percent, aqueous IPA solution, 33 mL). we injected  $\text{O}_2$  into the aqueous IPA solution for 60 min in dark, and the photocatalytic system was irradiated 300 W Xe Lamp.  $\text{H}_2\text{O}_2$  amount was measure by titration method with the acidic  $\text{KMnO}_4$  (0.2 mmol L<sup>-1</sup>) as titrant, and the amount of the reacted  $\text{KMnO}_4$  was the equal of  $\text{H}_2\text{O}_2$  evolution [13].

### 2.5. Photocatalytic elimination of HCHO and NO

HCHO elimination was carried out in 6 L quartz reactor at 25 °C under illumination. The reactor was vertically beamed through a Xe lamp (300 W) with a UV cutoff filter (420 nm). In accordance with our previous report [38], 0.1 g thin film of  $\text{Cu}/\text{C}_3\text{N}_4$  was prepared and installed to reaction generator. Typically, 0.1  $\text{Cu}/\text{C}_3\text{N}_4$  sample was uniformly dispersed into the deionized  $\text{H}_2\text{O}$  (15 mL) in a petri dish (7.0 cm d.) by ultrasonication for 25 min. The dispersed  $\text{Cu}/\text{C}_3\text{N}_4$  was dried at 60 °C for 1 h, obtaining thin film of  $\text{Cu}/\text{C}_3\text{N}_4$  on petri dish. Soon afterwards, the petri dish with the thin film was placed into the quartz reactor. Some volume of HCHO (38%) was imported to the reactor. After an adsorption/desorption balance in the darkness, initial content of HCHO was always maintained at ~200 ppm for each test. Under visible-light irradiation, HCHO,  $\text{CO}_2$ , and  $\text{H}_2\text{O}$  content was *in-situ* detected on a Photoacoustic IR multi-gas monitor. Meanwhile, the photocatalytic removal of NO gas was performed in the same photocatalytic system of HCHO elimination with using 600 ppb NO instead of 200 ppm HCHO. The content of NO was on-line surveyed with chemiluminescence NO analyzer. The removal efficiency (Y) of HCHO, and/or NO was evaluated in light of our previous report [39].

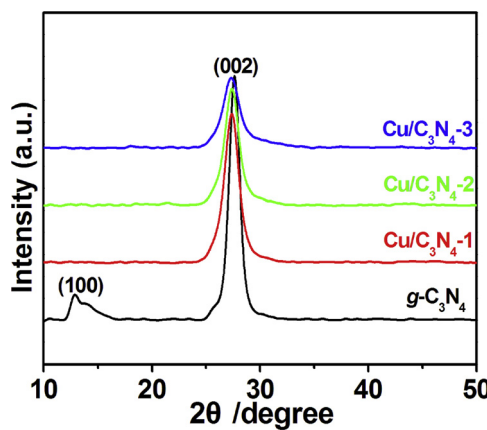


Fig. 1. XRD patterns of  $g\text{-C}_3\text{N}_4$  and  $\text{Cu/C}_3\text{N}_4$  samples.

### 3. Results and discussion

#### 3.1. Crystal composite and morphology

In Fig. 1, it is observed that XRD pattern of  $g\text{-C}_3\text{N}_4$  demonstrates the crystal diffraction characteristics of conjugated tri-s-triazine polymer, i.e., the pattern peak at  $13.1^\circ$  for diffraction plane of (100), and  $27.3^\circ$  for (002) [40–42]. The former plane represents the in-plane repetitive structure of tri-triazine, and the latter plane reflects the inter-layer stacking of the conjugated tri-s-triazine nanosheet [43,44]. For  $\text{Cu/C}_3\text{N}_4$  samples, it is seen that the diffraction signal at  $13.1^\circ$  almost vanishes, indicating that the in-plane repetitive structure of tri-triazine has been reduced, and the vacancy defect has been compensated [45–47]. Moreover, in comparison with the diffraction peak at  $27.6^\circ$  for  $g\text{-C}_3\text{N}_4$ , the peak of  $\text{Cu/C}_3\text{N}_4$  sample presents a obvious shift to  $27.2^\circ$ . In light of Bragg equation, inter-layer spacing is enlarged from  $0.322$  to  $0.327$  nm when Cu is introduced and coordinates with N of its vacancy structure. Additionally, it is observed that half peak width increases for  $\text{Cu/C}_3\text{N}_4$  samples, indicating the smaller grain size for  $\text{Cu/C}_3\text{N}_4$  samples compared with that of  $g\text{-C}_3\text{N}_4$ . The unoccupied orbits of  $\text{Cu}^{2+}$  interact with the N  $2p_z$  electrons of N at vacancy structure, which in certain degree inhibits hydrogen from bonding with N. Therefore, the Cu-coordinated N of tri-s-triazine nanosheet may inhibit the superposition of  $g\text{-C}_3\text{N}_4$  nanosheets [36,48], which results in the increase of interval spacing.

Then, the surface-chemical constituents, and their valences were examined by XPS. In the XPS spectra, the bound energies for all chemical components are calibrated on the basis of C 1s at  $284.8$  eV. In Fig. 2A, Cu  $2p_{3/2}$  signals of  $\text{Cu/C}_3\text{N}_4$  are observed at  $932.1$  eV, which are deservedly identified to be characteristic of Cu–N [49]. In Fig. 2B, O 1s signals for all samples  $g\text{-C}_3\text{N}_4$  demonstrate the two classified peaks at  $532.7$  and  $531.6$  eV, which can be considered as  $(\text{CN})_n\text{-O}$  and the adsorbed –OH species [6,50]. In Fig. 2C, N 1s spectra of  $g\text{-C}_3\text{N}_4$  and  $\text{Cu/C}_3\text{N}_4$  samples are fitted into  $\text{C}=\text{N}-\text{C}$  ( $398.4$  eV),  $\text{C}_3\text{N}$  and  $\text{Cu-N}$  ( $399.9$  eV), and  $\text{N-H}$  ( $401.2$  eV), respectively [39,43,51,52]. For  $\text{Cu/C}_3\text{N}_4$  samples, peak intensity of  $\text{N-H}$  species decreases, indicating the decrease of hydrogen bonding on the  $\text{Cu/C}_3\text{N}_4$  sample may weaken the superposition of  $g\text{-C}_3\text{N}_4$  nanosheets. C 1s signals for  $g\text{-C}_3\text{N}_4$  and  $\text{Cu/C}_3\text{N}_4$  are presented in Fig. 2D. The content of Cu in  $\text{Cu/C}_3\text{N}_4$  samples is  $0.18$  ( $\text{Cu/C}_3\text{N}_4\text{-1}$ ),  $0.33$  ( $\text{Cu/C}_3\text{N}_4\text{-2}$ ), and  $0.53$  wt.% ( $\text{Cu/C}_3\text{N}_4\text{-3}$ ) as detected by ICP-AES.

The chemical compositions and structures of  $\text{Cu/C}_3\text{N}_4$  samples were further detected by FT-IR spectra. In Fig. 3, all spectra demonstrate a clear signal at  $810\text{ cm}^{-1}$  which is the breathing mode of tri-s-triazine [50]. Signals at  $1200\text{--}1700\text{ cm}^{-1}$  ascribe to the vibration modes of C–N bonds in tri-s-triazine [53]. Furthermore, absorption at  $3000\text{--}3400\text{ cm}^{-1}$  belongs to the vibration mode of N–H bonds [50]. The FT-IR spectra results suggest that Cu coordination has not break the

$\pi$ -conjugated structure of tri-s-triazine polymer.

Cu-coordination influence on the image of  $\text{Cu/C}_3\text{N}_4$  has been probed through FESEM and TEM, and these results are demonstrated in Fig. 4A and B, and Fig. S1 of Supplementary data.  $\text{Cu/C}_3\text{N}_4$  samples present grenadine-like nanolayers with enormously smooth and fluffy-flocculation characteristic, while  $g\text{-C}_3\text{N}_4$  is made up of the accumulated and compact particles (Fig. S1). The fluffy-flocculation layers for  $\text{Cu/C}_3\text{N}_4$  was further characterized by FESEM-EDX (Fig. 4C–F), and EDX element mappings suggest a uniform of C, N, Cu, and O for  $\text{Cu/C}_3\text{N}_4$  sample. The grenadine-like layers with smooth and fluffy-flocculation characteristic supplies abundant reactive site and a large smooth surface for light trapping.

#### 3.2. Microstructures and surface physicochemical properties

Nitrogen adsorption/desorption isothermal curves and the deduced pore properties of  $g\text{-C}_3\text{N}_4$ , and  $\text{Cu/C}_3\text{N}_4$  are presented in Fig. 5A and B. All tests display type-IV isothermal curves with H3-hysteresis loops, suggesting the trait of slit-like mesopores [54]. On the one hand, Cu coordination with  $g\text{-C}_3\text{N}_4$  leads to the expanded  $\pi$ -conjugated structure by “patching” the vacancy of tri-s-triazine; on the other hand, interlayer spacing is enlarged. In comparison with  $g\text{-C}_3\text{N}_4$ ,  $\text{Cu/C}_3\text{N}_4$  samples show much higher adsorption quantity. BET specific surface areas are  $45$  ( $\text{Cu/C}_3\text{N}_4\text{-1}$ ),  $87$  ( $\text{Cu/C}_3\text{N}_4\text{-2}$ ), and  $138\text{ m}^2\text{ g}^{-1}$  ( $\text{Cu/C}_3\text{N}_4\text{-3}$ ), which is  $1.8$ ,  $3.48$ , and  $5.52$  times that of  $g\text{-C}_3\text{N}_4$  ( $25\text{ m}^2\text{ g}^{-1}$ ), respectively. Pore size by calculating by BJH method is  $10\text{--}15$  nm for  $g\text{-C}_3\text{N}_4$ , and  $\text{Cu/C}_3\text{N}_4$  samples, nevertheless,  $\text{Cu/C}_3\text{N}_4$  samples demonstrate larger pore volumes. The elaborate data of these physicochemical properties for all samples are shown in Table S1. The enlarged BET specific surface areas and pore volumes are beneficial to the adsorption of the reactants and the capture of light.

#### 3.3. DFT calculation for electronic structure of $\text{Cu/C}_3\text{N}_4$

DFT calculations were performed to examine Cu coordination effect on the geometry of  $g\text{-C}_3\text{N}_4$ . Fig. 6A presents an optimization process of  $\text{Cu/C}_3\text{N}_4$  geometry by  $\text{Cu}^{2+}$  coordination with different site of conjugated tri-s-triazine. When the vacant orbit of  $\text{Cu}^{2+}$  coordinates with electron of graphic-like N in  $g\text{-C}_3\text{N}_4$  (at site 1), the total energy is  $-2200.38$  (Hartree). For the coordination at site 2, and 3, total energy declines to  $-2200.41$ , and  $-2200.43$  (Hartree), respectively; it is noted that vacant orbits of  $\text{Cu}^{2+}$  spontaneously coordinate with six  $\text{sp}^2$ -hybridized N at vacancy of  $g\text{-C}_3\text{N}_4$  (at site 4), and the total energy reduces to  $-2200.48$  (Hartree). In this case, d– $\pi$  conjugation is formed by partial  $\pi$  electron cloud on the conjugated tri-s-triazine ring entering into the 3d orbit of  $\text{Cu}^{2+}$ , which makes  $\text{Cu}^{2+}$  to bond with the the conjugated tri-s-triazine firmly [55,56]. Therefore, it is clearly seen that the site 4 is thermodynamically advantageous for the coordination between  $\text{Cu}^{2+}$  and six  $\text{sp}^2$ -hybridized N atoms at vacancy of  $g\text{-C}_3\text{N}_4$ , resulting in patching vacancy and thus expanding the conjugated structure. Müllenken charge analysis was used to investigate the charge distribution over  $g\text{-C}_3\text{N}_4$  before and after coordination of  $\text{Cu}^{2+}$  with  $\text{sp}^2$ -hybridized N atoms at vacancy of tri-s-triazine nanosheet (Figs. 6B and S3). In Fig. 6B, it is seen that the difference between N and C atom around the Cu atom becomes smaller, and the distribution of electrons tends to be uniform, and electrons are preferentially concentrated around Cu, and C (linked with N of vacancy), suggesting that the effective-directional transfer of electrons is achieved over the expanded  $\pi$ -conjugated structure of  $\text{Cu/C}_3\text{N}_4$  sample. N  $2p_z$  orbitals of six  $\text{sp}^2$ -hybridized N atoms at vacancy sites overlap the unoccupied orbitals of  $\text{Cu}^{2+}$  (Fig. 6C), which will result in the efficient transfer of charge over  $\text{Cu/C}_3\text{N}_4$ . Moreover, the charge migration between adjacent layers is promoted by Cu sites, as reflected in the decrease of positive charge of Cu (Fig. 6D).

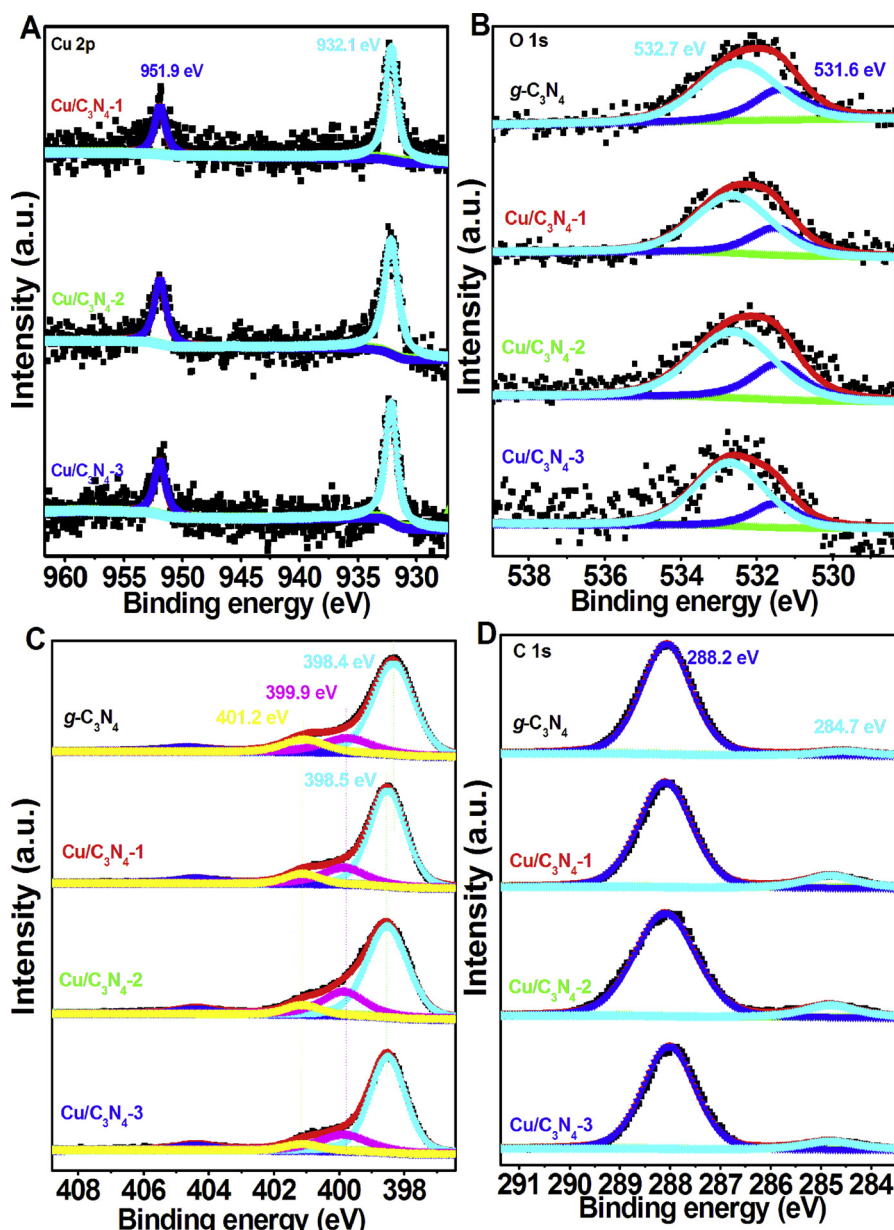


Fig. 2. XPS spectra of  $g\text{-C}_3\text{N}_4$  and  $\text{Cu/C}_3\text{N}_4$  samples, (A) Cu 2p, (B) O 1s, (C) N 1s, and (D) C 1s.

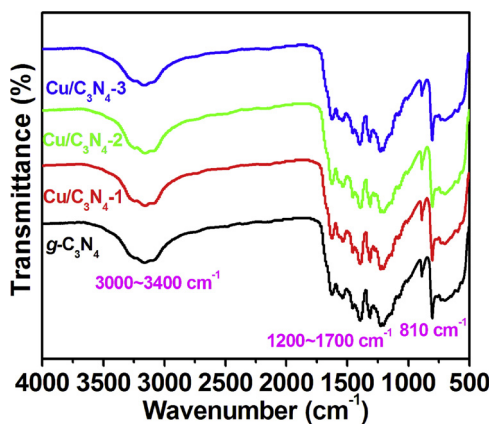


Fig. 3. FT-IR spectra of  $g\text{-C}_3\text{N}_4$  and  $\text{Cu/C}_3\text{N}_4$  samples.

#### 3.4. Optical and electrical properties

From the above series characterizations of components and structure, it is seen that  $\text{Cu}^{2+}$  coordinates with  $\text{sp}^2$ -hybridized N atoms at vacancy sites of the conjugated tri-s-triazine nanosheet, which thus perfects  $\pi$ -delocalization structure of  $g\text{-C}_3\text{N}_4$  and will improve its light absorption region and electronic structure. In Fig. 7A, it is seen that the light-absorption edge for  $g\text{-C}_3\text{N}_4$  is 424 nm. However, for  $\text{Cu/C}_3\text{N}_4$  samples, the absorption spectra demonstrate clearly a red shift with the strengthened light intensity, revealing that the as extended  $\pi$ -conjugated structure is conducive to light capturing due to  $\text{Cu}^{2+}$  coordination with  $\text{sp}^2$ -hybridized N at vacancy site of tri-s-triazine. Taking  $\text{Cu/C}_3\text{N}_4\text{-}3$  as an example, the absorption edge expands to 468 nm with the enhanced absorption from UV to near NIR. On the basis of photon energy vs.  $(\alpha h\nu)^{1/2}$ , band gaps ( $E_g$ ) is 2.73, 2.64, 2.54, and 2.41 eV corresponding successively to  $g\text{-C}_3\text{N}_4$ ,  $\text{Cu/C}_3\text{N}_4\text{-}1$ ,  $\text{Cu/C}_3\text{N}_4\text{-}2$ , and  $\text{Cu/C}_3\text{N}_4\text{-}3$  samples (Fig. S2). The narrowed band gaps for  $\text{Cu/C}_3\text{N}_4$  samples promote light absorption and photoelectron transition. Moreover, EPR curves of  $g\text{-C}_3\text{N}_4$ , and  $\text{Cu/C}_3\text{N}_4$  are detected in Fig. 7B, and  $g$  values are

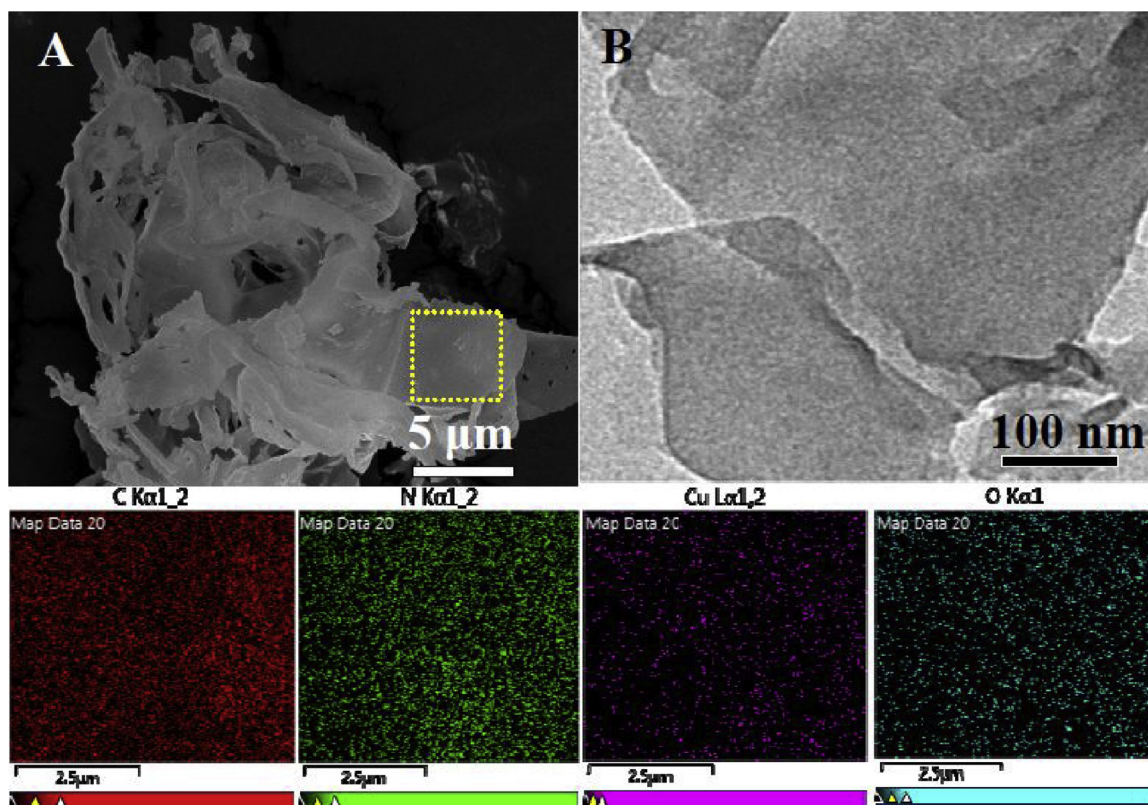


Fig. 4. FESEM, TEM, and element mapping of Cu/C<sub>3</sub>N<sub>4</sub>-3.

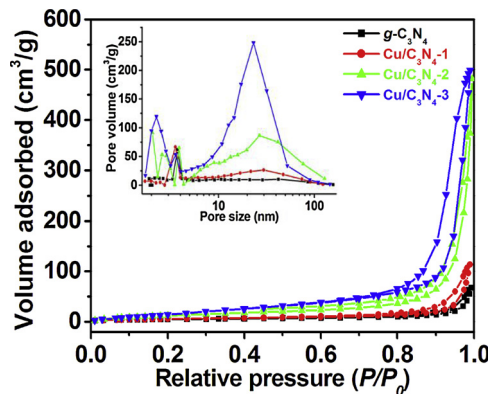


Fig. 5. Nitrogen adsorption/desorption isothermal curves and the deduced pore properties of g-C<sub>3</sub>N<sub>4</sub>, and Cu/C<sub>3</sub>N<sub>4</sub> samples.

at 2.0000, which induces by lone electrons of the  $\pi$ -conjugated structure [53]. Cu/C<sub>3</sub>N<sub>4</sub> samples exhibit the signals of EPR at 2.0000 with higher intensity, suggesting that the increased degree of delocalization [57]. In addition, time-resolved fluorescence spectra of g-C<sub>3</sub>N<sub>4</sub>, and Cu/C<sub>3</sub>N<sub>4</sub>-3 samples were recorded by fitting with bi-exponential functions (Fig. 7C). Fast- and long-fluorescence decay spectra are essentially due to the non-radiative and radiative processes [53,58], respectively. Non-radiative step reflects the defect structure of semiconductor, and radiative step shows the recombination process of e<sup>-</sup> and h<sup>+</sup> [6,39,59]. In Fig. 7C, short lifetime ( $\tau_1$ ) for fast-fluorescence decay 1.2, 1.7, 2.2, and 2.5 ns, and the long lifetime ( $\tau_2$ ) for long-fluorescence decay is 5.8, 6.3, 6.8, and 7.3 ns, which corresponds to g-C<sub>3</sub>N<sub>4</sub>, Cu/C<sub>3</sub>N<sub>4</sub>-1, Cu/C<sub>3</sub>N<sub>4</sub>-2, and Cu/C<sub>3</sub>N<sub>4</sub>-3, respectively. The percent of the non-radiation step reduces with the extended short lifetime for Cu/C<sub>3</sub>N<sub>4</sub>-3 in comparison with that for g-C<sub>3</sub>N<sub>4</sub>, suggesting the decrease of defect structure for Cu/C<sub>3</sub>N<sub>4</sub> as a result of coordination between Cu<sup>2+</sup> 3d with N 2p<sub>z</sub> electron of

vacancy of tri-s-triazine nanosheet. Meanwhile, the extended  $\pi$ -conjugated structure boosts the charge transfer of Cu/C<sub>3</sub>N<sub>4</sub>, which presents as the extended-long lifetime and normal radiation percent. In the EIS-Nyquist characterization (Fig. 7D), the semicircle curves originate from charge transportation between electrode and electrolyte [60]. Cu/C<sub>3</sub>N<sub>4</sub> samples demonstrate smaller electric-resistance compared with g-C<sub>3</sub>N<sub>4</sub>, stating clearly that Cu/C<sub>3</sub>N<sub>4</sub> samples efficiently promotes electron transfer. Under light irradiation, photoelectron over sample transports into its back contact and interacts with electrolyte to produce photocurrent [61], as shown in the i-t patterns (Fig. 7E), obviously, the highest anodic photocurrent intensity is achieved on Cu/C<sub>3</sub>N<sub>4</sub>-3. When O<sub>2</sub> interacts with Cu/C<sub>3</sub>N<sub>4</sub>, photoelectron is preferentially trapped with O<sub>2</sub>, which therefore impels h<sup>+</sup> diffusion on the surface of electrode, forming SPS signals. Accordingly, the signal intensity is proportional to the efficiency of charge transfer and utilization [62,63], and Cu/C<sub>3</sub>N<sub>4</sub>-3 reflects optimal efficiency of photo-irradiated charge transportation (Fig. 7F). As a result, photo-irradiated charge transfer over Cu/C<sub>3</sub>N<sub>4</sub> samples will be preferentially transferred to the dissolved O<sub>2</sub> to evolve ROS in the aqueous oxygen system under light irradiation.

### 3.5. Photocatalytic performance

EPR was performed to examine active oxygen species, and DMPO was developed to test ·OH and ·O<sub>2</sub><sup>-</sup> by detecting the corresponding signals, respectively. In Fig. 8A, EPR patterns of DMPO-·O<sub>2</sub><sup>-</sup> with peak intensity ratio of 1:1:1:1 are exhibited [64,65], and the much obvious DMPO-·O<sub>2</sub><sup>-</sup> peaks are achieved for Cu/C<sub>3</sub>N<sub>4</sub> samples, however, for g-C<sub>3</sub>N<sub>4</sub>, the peak intensity is relative weaker. Besides, ·OH signals with the ratio of 1:2:2:1 are hardly tested for g-C<sub>3</sub>N<sub>4</sub>, and Cu/C<sub>3</sub>N<sub>4</sub> samples (Fig. 8B) [6,50,64]. Therefore, ·O<sub>2</sub><sup>-</sup> can be photocatalytically yielded over g-C<sub>3</sub>N<sub>4</sub>, and Cu/C<sub>3</sub>N<sub>4</sub> samples, which is consistent with the CB and VB potentials of g-C<sub>3</sub>N<sub>4</sub>, and Cu/C<sub>3</sub>N<sub>4</sub>. In Fig. S4, it is seen that CB potentials for g-C<sub>3</sub>N<sub>4</sub>, and Cu/C<sub>3</sub>N<sub>4</sub> satisfy thermodynamic requirement from O<sub>2</sub> to ·O<sub>2</sub><sup>-</sup>, however VB potentials are not suitable for

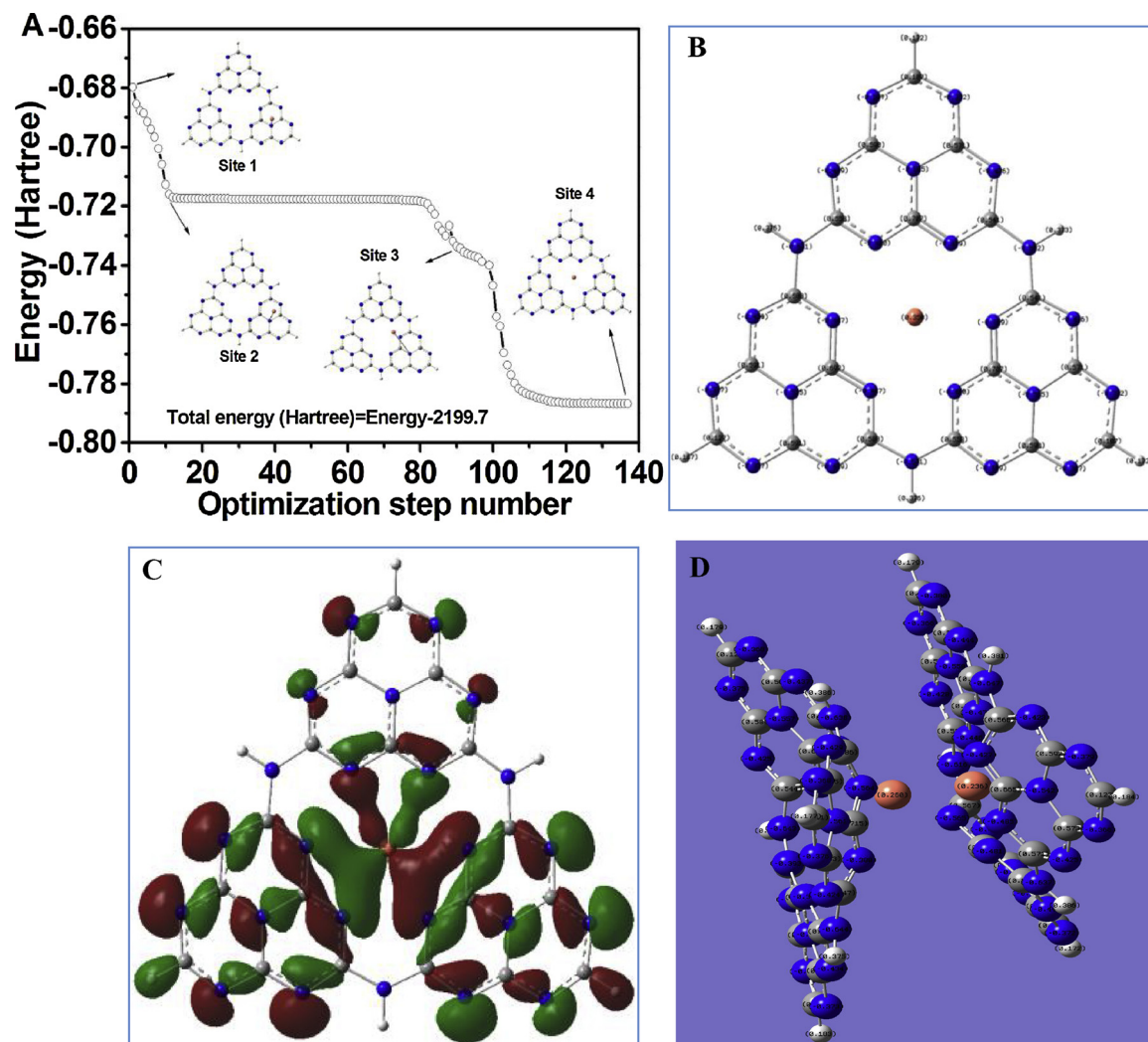


**Fig. 6.** The optimization process of Cu/C<sub>3</sub>N<sub>4</sub> geometry by Cu coordination with different site of conjugated tri-s-triazine (A), Mulliken charge distribution over monolayer Cu/C<sub>3</sub>N<sub>4</sub> (B), the corresponding overlap of 2p<sub>z</sub> orbitals of N at vacancy sites and Cu<sup>2+</sup> 3d orbitals (C), and Mulliken charge distribution between adjacent-layer Cu/C<sub>3</sub>N<sub>4</sub> (D).

requirement of ·OH evolution. In addition, the photocatalytic amount of O<sub>2</sub><sup>−</sup> is tested by NBT transform method [66,67]. As shown in Fig. S5, absorption peak at 259 nm gradually declines in photoluminescence of NBT, indicating that NBT is consistently oxidized with O<sub>2</sub><sup>−</sup> over Cu/C<sub>3</sub>N<sub>4</sub>-3 sample. On the basis of reaction molar ratio (n(NBT)/n(O<sub>2</sub><sup>−</sup>) = 1:4), O<sub>2</sub><sup>−</sup> production is 3, 5, 9, and 13 μmol L<sup>−1</sup> h<sup>−1</sup> over g-C<sub>3</sub>N<sub>4</sub>, Cu/C<sub>3</sub>N<sub>4</sub>-1, Cu/C<sub>3</sub>N<sub>4</sub>-2, and Cu/C<sub>3</sub>N<sub>4</sub>-3 (Fig. 8C), respectively, and the optimal photocatalytic efficiency for O<sub>2</sub><sup>−</sup> evolution is completed over Cu/C<sub>3</sub>N<sub>4</sub>-3. In Fig. 8D, effect of irradiation time on O<sub>2</sub><sup>−</sup> efficiency with g-C<sub>3</sub>N<sub>4</sub> and Cu/C<sub>3</sub>N<sub>4</sub> sample as photocatalyst is displayed, and continuing O<sub>2</sub><sup>−</sup> yield is observed with no decline of evolution efficiency, nevertheless, the performance trend diagram vs. time is obviously different over g-C<sub>3</sub>N<sub>4</sub> and Cu/C<sub>3</sub>N<sub>4</sub> samples. After 120 min reaction, O<sub>2</sub><sup>−</sup> evolution efficiency increases slowly over g-C<sub>3</sub>N<sub>4</sub>, while the photocatalytic efficiency maintains high rates for Cu/C<sub>3</sub>N<sub>4</sub> samples, specially for Cu/C<sub>3</sub>N<sub>4</sub>-3, the fast increase of O<sub>2</sub><sup>−</sup> efficiency can be obtained. The results of the enhanced photocatalytic activity for O<sub>2</sub><sup>−</sup> evolution over Cu/C<sub>3</sub>N<sub>4</sub> can be achieved due to the formation of extended π-conjugated structure by coordinating Cu<sup>2+</sup> with N 2p<sub>z</sub> of tri-s-triazine nanosheet in combination with the above series characterizations.

Besides, Cu/C<sub>3</sub>N<sub>4</sub> samples display high activity for H<sub>2</sub>O<sub>2</sub> evolution, and the results are shown in Fig. 8E. H<sub>2</sub>O<sub>2</sub> evolution efficiency over Cu/C

C<sub>3</sub>N<sub>4</sub> samples is greatly higher than that over g-C<sub>3</sub>N<sub>4</sub> (200 μmol L<sup>−1</sup> h<sup>−1</sup>). For Cu/C<sub>3</sub>N<sub>4</sub> samples, H<sub>2</sub>O<sub>2</sub> evolution efficiency over Cu/C<sub>3</sub>N<sub>4</sub>-1, Cu/C<sub>3</sub>N<sub>4</sub>-2, and Cu/C<sub>3</sub>N<sub>4</sub>-3 is 389, 460, and 550 μmol L<sup>−1</sup> h<sup>−1</sup>. Cu/C<sub>3</sub>N<sub>4</sub>-3 sample possesses the optimal efficiency which is 2.75 times that of g-C<sub>3</sub>N<sub>4</sub> under light irradiation with same wavelength. These photocatalytic performances state clearly that the coordination of Cu<sup>2+</sup> with N 2p<sub>z</sub> of vacancy structure of g-C<sub>3</sub>N<sub>4</sub> promotes H<sub>2</sub>O<sub>2</sub> photosynthesis. In Fig. S10, influence of illumination time on H<sub>2</sub>O<sub>2</sub> efficiency over all samples is also investigated, and sustainable H<sub>2</sub>O<sub>2</sub> yield is achieved with no decline, nevertheless, the efficiency-trend diagram vs. time is clearly diversity over g-C<sub>3</sub>N<sub>4</sub> and Cu/C<sub>3</sub>N<sub>4</sub> samples. In the 120 min of photocatalytic reaction process, H<sub>2</sub>O<sub>2</sub> production efficiency enhances mildly over g-C<sub>3</sub>N<sub>4</sub>, while the efficiency demonstrates the high rates for Cu/C<sub>3</sub>N<sub>4</sub> samples, indicating the sustainable evolution capability of H<sub>2</sub>O<sub>2</sub> over the extended π-conjugated structure. Additionally, excitation-wavelength effect on H<sub>2</sub>O<sub>2</sub> efficiency over Cu/C<sub>3</sub>N<sub>4</sub>-3 is also probed, Fig. 8F demonstrates the continuous H<sub>2</sub>O<sub>2</sub> evolution with 240 and 75 μmol L<sup>−1</sup> h<sup>−1</sup> over Cu/C<sub>3</sub>N<sub>4</sub>-3 under visible light (560 nm) and near infrared light ( $\geq 780$  nm) irradiation, respectively. On the other hand, no H<sub>2</sub>O<sub>2</sub> was observed when g-C<sub>3</sub>N<sub>4</sub> was used as photocatalyst (Fig. S6). Moreover, H<sub>2</sub>O<sub>2</sub> efficiency over Cu/C<sub>3</sub>N<sub>4</sub>-3 is coincident with its absorption spectrum. Therefore, the Cu/C<sub>3</sub>N<sub>4</sub>-3 performs well in the visible and near infrared region, promising the more efficient utilization

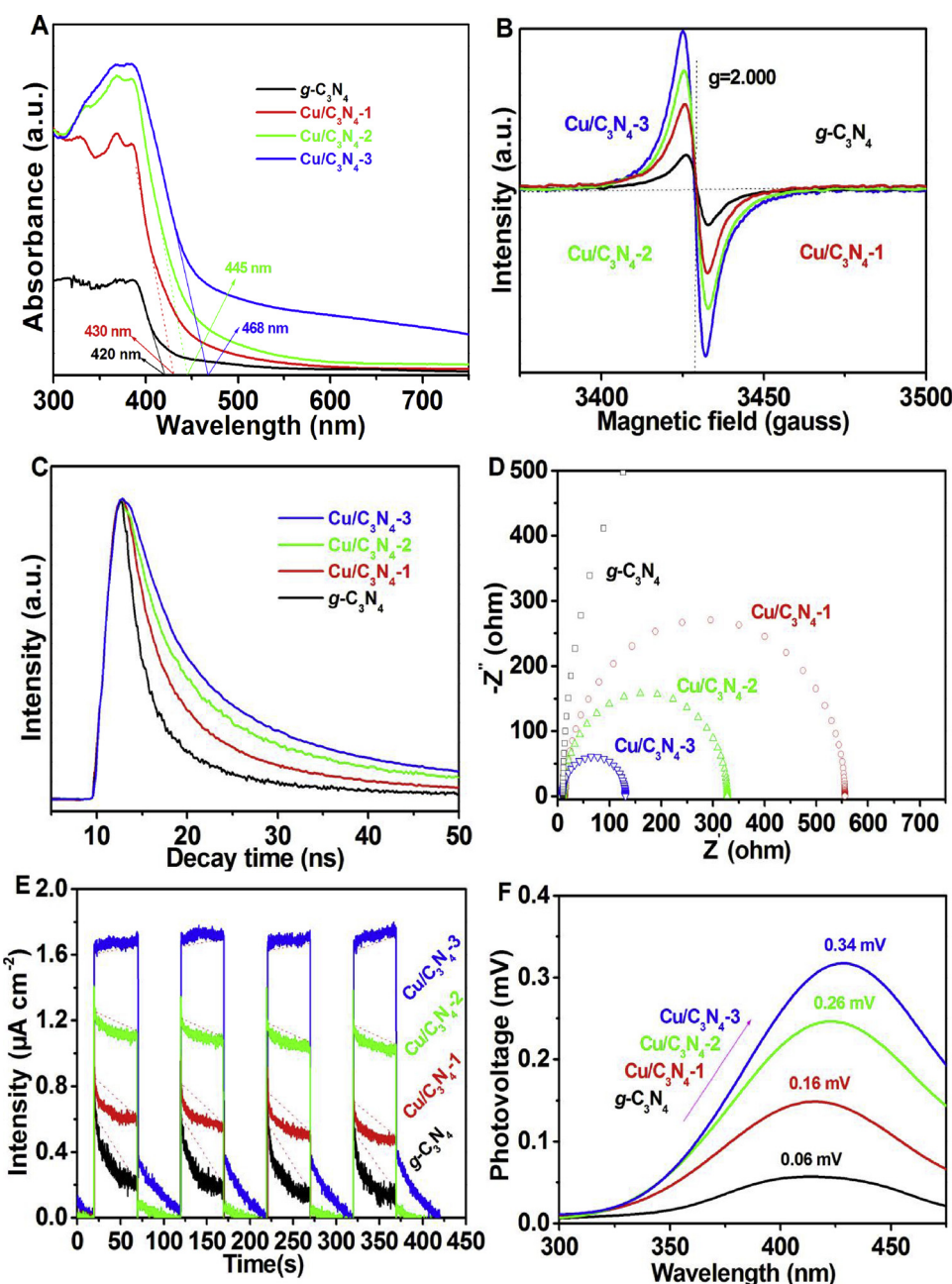


**Fig. 7.** UV-vis spectra (A), EPR patterns (B), time-resolved fluorescence spectra (C), electrochemical impedance spectra (D), transient photocurrent response (E), and surface photovoltage spectra (F) of  $g\text{-C}_3\text{N}_4$  and  $\text{Cu/C}_3\text{N}_4$  samples.

of long-wavelength solar energy in comparison with  $g\text{-C}_3\text{N}_4$ . In connection with the  $\text{O}_2^-$  evolution efficiency, it is concluded that the improved  $\pi$ -conjugated structure of  $\text{Cu/C}_3\text{N}_4$  with the optimized electron structure promotes the efficiently sustainable evolution of  $\text{O}_2^-$  and  $\text{H}_2\text{O}_2$ .

In consideration of importance of reactive oxygen species in the environment,  $\text{Cu/C}_3\text{N}_4$  samples were as well performed to decontaminate NO, and HCHO pollutants, and the results are displayed in Fig. 9. Only 52 ppm of HCHO was eliminated in the presence of  $g\text{-C}_3\text{N}_4$ , which is due to the severe recombination of photo-induced  $e^-$  and  $h^+$ . After coordinating N 2p lone electrons of vacancy of tri-s-triazine with vacant orbits of  $\text{Cu}^{2+}$ , elimination efficiency of HCHO greatly enhances, specifically, HCHO content declines from 200 ppm to 79, 53, and 29 for  $\text{Cu/C}_3\text{N}_4\text{-}1$ ,  $\text{Cu/C}_3\text{N}_4\text{-}2$ ,  $\text{Cu/C}_3\text{N}_4\text{-}3$ , respectively (Fig. 9A). Correspondingly,  $\text{CO}_2$  content increases to 77, 178, 216, and 251 ppm for  $g\text{-C}_3\text{N}_4$ ,  $\text{Cu/C}_3\text{N}_4\text{-}1$ ,  $\text{Cu/C}_3\text{N}_4\text{-}2$ , and,  $\text{Cu/C}_3\text{N}_4\text{-}3$ , respectively (Fig. 9B).

Moreover,  $\text{Cu/C}_3\text{N}_4$  samples demonstrate high stability in the recycle tests for HCHO elimination (Fig. S7). In the photocatalytic removal of NO,  $\text{Cu/C}_3\text{N}_4$  samples also display better catalytic efficiency than  $g\text{-C}_3\text{N}_4$ , i.e., 30.2 ( $g\text{-C}_3\text{N}_4$ ), 44.3 ( $\text{Cu/C}_3\text{N}_4\text{-}1$ ), 61.2 ( $\text{Cu/C}_3\text{N}_4\text{-}2$ ), and 108  $\mu\text{mol L}^{-1}\text{ h}^{-1}$  ( $\text{Cu/C}_3\text{N}_4\text{-}3$ ), and the removal efficiency of NO over the optimal  $\text{Cu/C}_3\text{N}_4$  is 3.57 times of that over  $g\text{-C}_3\text{N}_4$ . Previous reports confirm that elimination efficiency of HCHO and NO over  $g\text{-C}_3\text{N}_4$  is closely related to the photocatalytic yield of ROS [39], which confirms the great importance of ROS over  $\text{Cu/C}_3\text{N}_4$  for environmental purification.

Whereafter, the photocatalytic principles of  $\text{O}_2^-$ , and  $\text{H}_2\text{O}_2$  production over  $g\text{-C}_3\text{N}_4$ , and  $\text{Cu/C}_3\text{N}_4$  are probed. In Fig. 10,  $\text{N}_2$  (99.999%) was used to consume the dissolved  $\text{O}_2$  in the photocatalytic system of ROS evolution. It is seen that  $\text{H}_2\text{O}_2$  yield for  $g\text{-C}_3\text{N}_4$  and  $\text{Cu/C}_3\text{N}_4\text{-}3$  can not be completely vanished, stating clearly that  $\text{H}_2\text{O}_2$  production is not merely by photocatalytically reducing the dissolved  $\text{O}_2$  with photo-

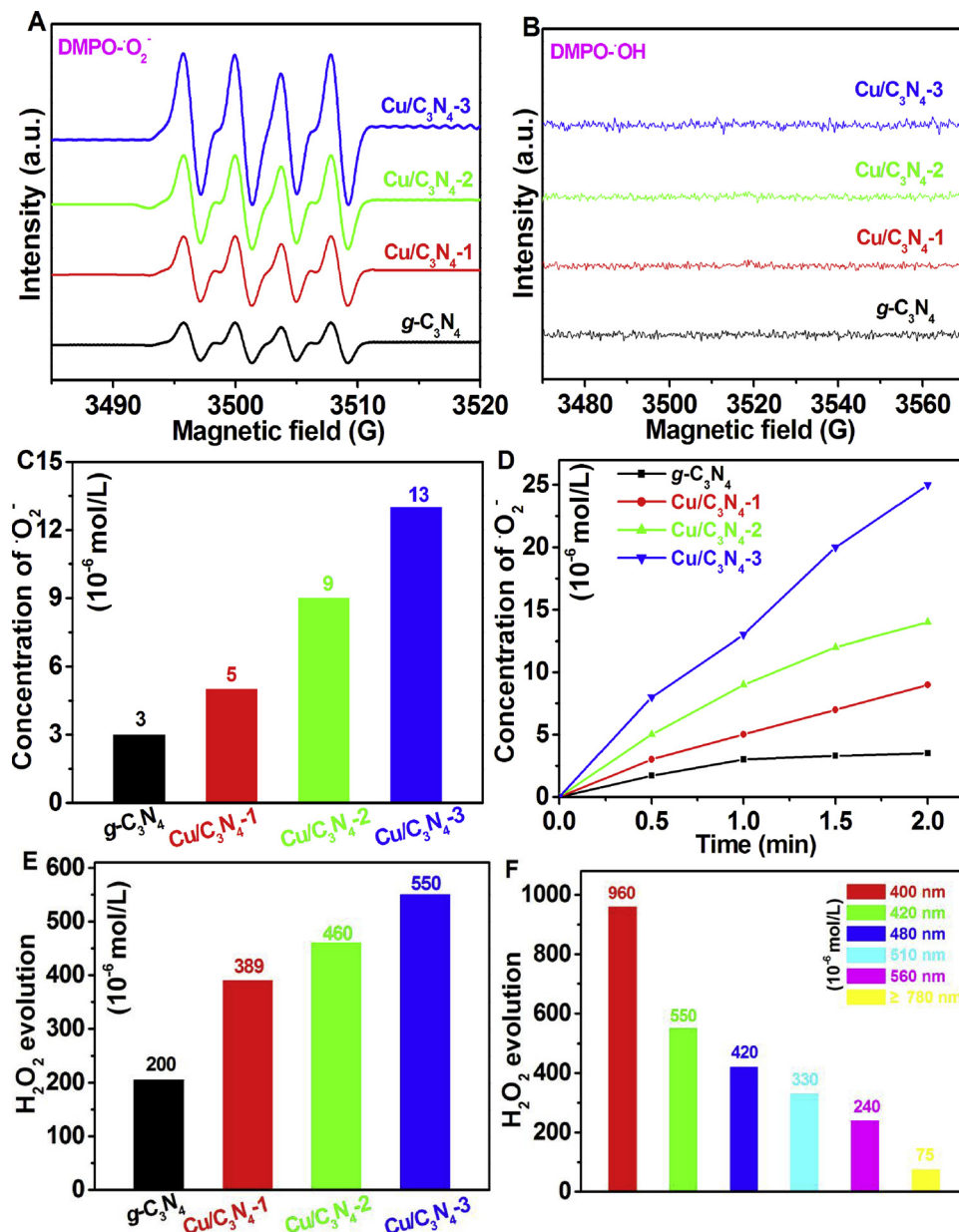


**Fig. 8.** EPR spectra of DMPO-·O<sub>2</sub><sup>-</sup> in the methanol dispersion solution (A), DMPO-·OH in aqueous dispersion (B) over g-C<sub>3</sub>N<sub>4</sub>, and Cu/C<sub>3</sub>N<sub>4</sub> samples, yield efficiency of ·O<sub>2</sub><sup>-</sup> (C), and H<sub>2</sub>O<sub>2</sub> (E), time- and wavelength-dependent effects on the efficiency of ·O<sub>2</sub><sup>-</sup> (D), and H<sub>2</sub>O<sub>2</sub> (F), respectively.

induced e<sup>-</sup>. A small quantity of H<sub>2</sub>O<sub>2</sub> is produced under N<sub>2</sub> bubbling for g-C<sub>3</sub>N<sub>4</sub>, and Cu/C<sub>3</sub>N<sub>4</sub>-3, because the photo-induced h<sup>+</sup> of g-C<sub>3</sub>N<sub>4</sub> and Cu/C<sub>3</sub>N<sub>4</sub> oxidizes H<sub>2</sub>O into O<sub>2</sub> for compensating the dissolved oxygen, and 12.7 μmol h<sup>-1</sup> for O<sub>2</sub> evolution over Cu/C<sub>3</sub>N<sub>4</sub>-3 has been achieved in the presence of AgNO<sub>3</sub>. H<sub>2</sub>O<sub>2</sub> evolution efficiency for Cu/C<sub>3</sub>N<sub>4</sub>-3 is greatly higher than that for g-C<sub>3</sub>N<sub>4</sub>, indicating the effective utilization of h<sup>+</sup> over Cu/C<sub>3</sub>N<sub>4</sub>-3. The results also reveal that the efficient charge transfer is achieved on Cu/C<sub>3</sub>N<sub>4</sub>-3. Moreover, the improved hydrophilicity of Cu/C<sub>3</sub>N<sub>4</sub>-3 favors H<sub>2</sub>O adsorption and oxidation, which is also confirmed by hydrophilicity test results in the Fig. S8. It is seen that the H<sub>2</sub>O contact angle decreases from 43.3 (g-C<sub>3</sub>N<sub>4</sub>) to 21.5 (Cu/C<sub>3</sub>N<sub>4</sub>-3). When H<sub>2</sub>PtCl<sub>6</sub> is utilized to delete photo-induced e<sup>-</sup>, H<sub>2</sub>O<sub>2</sub> was not detected for g-C<sub>3</sub>N<sub>4</sub>, and Cu/C<sub>3</sub>N<sub>4</sub>-3. In photocatalytic H<sub>2</sub>O<sub>2</sub> evolution process, H<sub>2</sub>O<sub>2</sub> is achieved by O<sub>2</sub><sup>-</sup> reduction with e<sup>-</sup>. Due to coordinating Cu<sup>2+</sup> with N 2p<sub>z</sub> of vacancy of tri-s-triazine nanosheet, the charge distribution is homogenized, and the electronegativity difference between C and N is decreased over the extended π-conjugated structure of Cu/C<sub>3</sub>N<sub>4</sub>, thus greatly promoting the effective

transfer of photo-induced charge carriers. In the visible-light irradiation process, photo-induced e<sup>-</sup> conveniently reacts with O<sub>2</sub>, which produces O<sub>2</sub><sup>-</sup>. Afterwards, the photocatalytically produced O<sub>2</sub><sup>-</sup> further interacts with e<sup>-</sup> and H<sup>+</sup>, as a result producing H<sub>2</sub>O<sub>2</sub>. The detailed photosynthesis process of ROS is displayed in the inset of Fig. 10.

#### 4. Conclusion

In summary, efficient photocatalytic system for yielding reactive oxygen species over the extended π-delocalization Cu/C<sub>3</sub>N<sub>4</sub> photocatalysts have been designed by coordinating the vacancy of tri-s-triazine polymer with Cu 3d orbit. Cu/C<sub>3</sub>N<sub>4</sub> photocatalysts exhibit great performance for evolving O<sub>2</sub><sup>-</sup>, and H<sub>2</sub>O<sub>2</sub>. High efficiency over Cu/C<sub>3</sub>N<sub>4</sub> principally arises from the facilitating role of the extended π-delocalization structure. The extended π-delocalization structure of Cu/C<sub>3</sub>N<sub>4</sub> results in i) the strengthened harvesting capability from UV-NIR, ii) the efficient charge transfer ability from intrinsic material to O<sub>2</sub> molecular at sites of C (in C<sub>3</sub>-N) and Cu. In the removal process of HCHO, and NO,

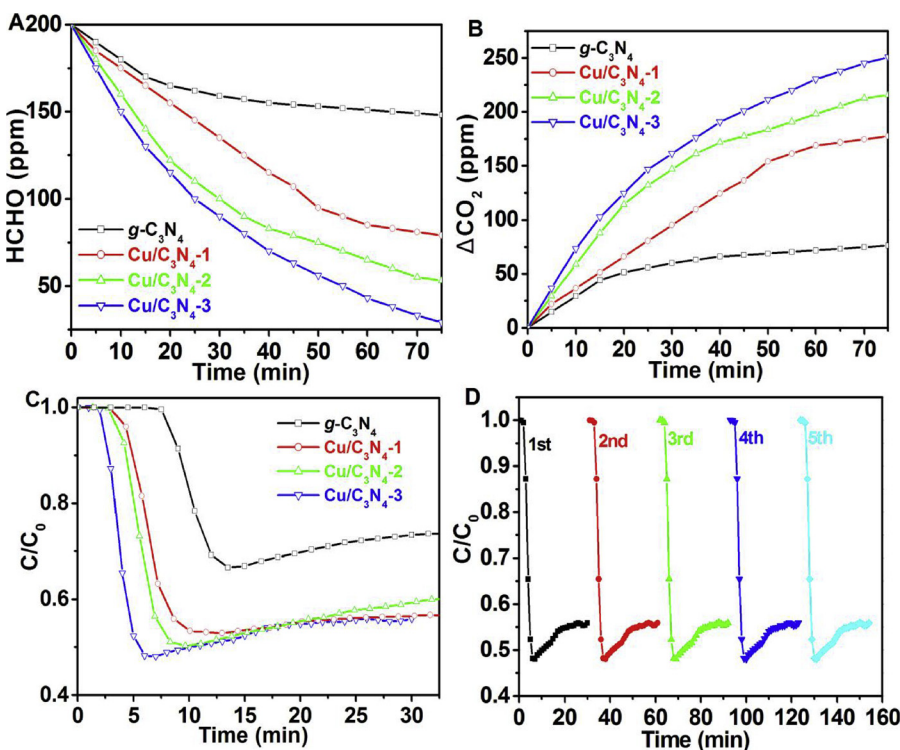


**Fig. 9.** Elimination efficiency for HCHO (A), and NO (C), the conversion performance from HCHO to CO<sub>2</sub> (B), and the recycles test for NO elimination (D) over  $g\text{-C}_3\text{N}_4$  and Cu/C<sub>3</sub>N<sub>4</sub> samples.

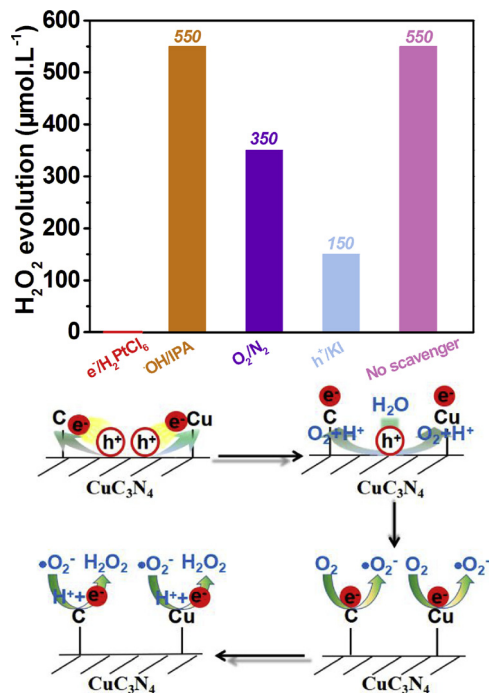


**Fig. 10.** The effect of scavengers (H<sub>2</sub>PtCl<sub>6</sub>, KI, IPA, N<sub>2</sub> for e<sup>-</sup>, h<sup>+</sup>, ·OH, O<sub>2</sub>, respectively) on H<sub>2</sub>O<sub>2</sub> yield over Cu/C<sub>3</sub>N<sub>4</sub>-3, and the corresponding mechanism for photocatalytic evolution of O<sub>2</sub><sup>-</sup> and H<sub>2</sub>O<sub>2</sub>.

Cu/C<sub>3</sub>N<sub>4</sub> photocatalysts demonstrate high and sustainable removal efficiency. The highly active photocatalytic system over the extended  $\pi$ -delocalization  $g\text{-C}_3\text{N}_4$  photocatalysts constructed by the convenient and low cost strategy demonstrates a promising application prospect for sustainable evolution and utilization of solar fuel.

## Acknowledgments

Our work was supported by NSFC (51462002, and 21871155), the Foundation of State key Laboratory Breeding Base of Nuclear Resources and Environment (Z201408 and Z1604).

## Appendix A. Supplementary data

Supplementary material related to this article can be found, in the online version, at doi:<https://doi.org/10.1016/j.apcatb.2019.03.014>.

## References

- [1] S.O. Ganiyu, M.H. Zhou, C.A. Martinez-Huitle, Heterogeneous electro-Fenton and photoelectro-Fenton processes: a critical review of fundamental principles and application for water/wastewater treatment, *Appl. Catal. B: Environ.* 235 (2018) 103–129.
- [2] P. Ganguly, C. Byrne, A. Breen, S.C. Pillai, Antimicrobial activity of photocatalysts: fundamentals, mechanisms, kinetics and recent advances, *Appl. Catal. B: Environ.* 225 (2018) 51–75.
- [3] Y. Nosaka, A.Y. Nosaka, Generation and detection of reactive oxygen species in photocatalysis, *Chem. Rev.* 117 (2017) 11302–11336.
- [4] T. Bak, J. Nowotny, N.J. Sucher, E. Wachsman, Effect of crystal imperfections on reactivity and photoreactivity of TiO<sub>2</sub> (Rutile) with oxygen, water, and bacteria, *J. Phys. Chem. C* 115 (2011) 15711–15738.
- [5] N. Waikopf, Y. Ben-Shahar, M. Galchenko, I. Carmel, G. Moshitzky, H. Soreq, U. Banin, Photocatalytic reactive oxygen species formation by semiconductor-metal hybrid nanoparticles. Toward light-induced modulation of biological processes, *Nano Lett.* 16 (2016) 4266–4273.
- [6] C.B. Xiong, S.J. Jiang, S.Q. Song, X. Wu, J.H. Li, Z.G. Le, Solid-solution-like o-C<sub>3</sub>N<sub>4</sub>/Ag<sub>2</sub>SO<sub>4</sub> nanocomposite as a direct Z-scheme photocatalytic system for photo-synthesis of active oxygen species, *ACS Sustain. Chem. Eng.* 6 (2018) 10905–10913.
- [7] S.Q. Huang, Y.G. Xu, Q.Q. Liu, T. Zhou, Y. Zhao, L.Q. Jing, H. Xu, H.M. Li, Enhancing reactive oxygen species generation and photocatalytic performance via adding oxygen reduction reaction catalysts into the photocatalysts, *Appl. Catal. B: Environ.* 218 (2017) 174–185.
- [8] P. Chen, F.L. Wang, Z.F. Chen, Q.X. Zhang, Y.H. Su, L.Z. Shen, K. Yao, Y. Liu, Z.W. Cai, W.Y. Lv, G.G. Liu, Study on the photocatalytic mechanism and detoxicity of gemfibrozil by a sunlight-driven TiO<sub>2</sub>/carbon dots photocatalyst: The significant roles of reactive oxygen species, *Appl. Catal. B: Environ.* 204 (2017) 250–259.
- [9] H.X. Zhao, X.Y. Chen, X.T. Li, C. Shen, B.C. Qu, J.S. Gao, J.W. Chen, X. Quan, Photoinduced formation of reactive oxygen species and electrons from metal oxide-silica nanocomposite: an EPR spin-trapping study, *Appl. Surf. Sci.* 416 (2017) 281–287.

- [10] Y.Y. Qin, H. Li, J. Lu, Y.S. Yan, Z.Y. Lu, X.L. Liu, Enhanced photocatalytic performance of  $\text{MoS}_2$  modified by  $\text{AgVO}_3$  from improved generation of reactive oxygen species, *Chin. J. Catal.* 39 (2018) 1470–1483.
- [11] J.Y. Gong, C.S. Lee, E.J. Kim, J.H. Kim, W. Lee, Y.S. Chang, Self-generation of reactive oxygen species on crystalline  $\text{AgBiO}_3$  for the oxidative remediation of organic pollutants, *ACS Appl. Mater. Interfaces* 9 (2017) 28426–28432.
- [12] S.Q. Song, A.Y. Meng, S.J. Jiang, B. Cheng, Three-dimensional hollow graphene efficiently promotes electron transfer of  $\text{Ag}_3\text{PO}_4$  for photocatalytically eliminating phenol, *Appl. Surf. Sci.* 442 (2018) 224–231.
- [13] Y. Zheng, Z.H. Yu, H.H. Ou, A.M. Asiri, Y.L. Chen, X.C. Wang, Black phosphorous and polymeric carbon nitride heterostructure for photoinduced molecular oxygen activation, *Adv. Funct. Mater.* 28 (2018) 1705407.
- [14] J. Li, L.J. Cai, J. Shang, Y. Yu, L.Z. Zhang, Giant enhancement of internal electric field boosting bulk charge separation for photocatalysis, *Adv. Mater.* 28 (2016) 4059–4064.
- [15] M.R. Hoffmann, S.T. Martin, W.Y. Choi, D.W. Bahnemann, Environmental applications of semiconductor photocatalysis, *Chem. Rev.* 95 (1995) 69–96.
- [16] H.W. Huang, S.C. Tu, C. Zeng, T.R. Zhang, A.H. Reshak, Y.H. Zhang, Macroscopic polarization enhancement promoting photo- and piezoelectric-induced charge separation and molecular oxygen activation, *Angew. Chem. Int. Ed.* 56 (2017) 11860–11864.
- [17] Z.J. Li, Y.B. Luan, Y. Qu, L.Q. Jing, Modification strategies with inorganic acids for efficient photocatalysts by promoting the adsorption of  $\text{O}_2$ , *ACS Appl. Mater. Interfaces* 7 (2015) 22727–22740.
- [18] J.W. Fu, J.G. Yu, C.J. Jiang, B. Cheng,  $\text{g-C}_3\text{N}_4$ -based heterostructured photocatalysts, *Adv. Energy Mater.* 8 (2018) 1701503.
- [19] S.W. Cao, J.X. Low, J.G. Yu, M. Jaroniec, Polymeric photocatalysts based on graphitic carbon nitride, *Adv. Mater.* 27 (2015) 2150–2176.
- [20] G. Mamba, A.K. Mishra, Graphitic carbon nitride ( $\text{g-C}_3\text{N}_4$ ) nanocomposites: a new and exciting generation of visible light driven photocatalysts for environmental pollution remediation, *Appl. Catal. B: Environ.* 198 (2016) 347–377.
- [21] X.L. Liu, P. Wang, H.S. Zhai, Q.Q. Zhang, B.B. Huang, Z.Y. Wang, Y.Y. Liu, Y. Dai, X.Y. Qin, X.Y. Zhang, Synthesis of synergistic phosphorus and cyano groups (CN) modified  $\text{g-C}_3\text{N}_4$  for enhanced photocatalytic  $\text{H}_2$  production and  $\text{CO}_2$  reduction under visible light irradiation, *Appl. Catal. B: Environ.* 232 (2018) 521–530.
- [22] H.L. Li, F.P. Li, Z.Y. Wang, Y.C. Jiao, Y.Y. Liu, P. Wang, X.Y. Zhang, X.Y. Qin, B.B. Huang, Fabrication of carbon bridged  $\text{g-C}_3\text{N}_4$  through supramolecular self-assembly for enhanced photocatalytic hydrogen evolution, *Appl. Catal. B: Environ.* 229 (2018) 114–120.
- [23] W.J. Wang, H.F. Cheng, B.B. Huang, X.L. Liu, X.Y. Qin, X.Y. Zhang, Y. Dai, Hydrothermal synthesis of  $\text{C}_3\text{N}_4/\text{BiOIO}_3$  heterostructures with enhanced photocatalytic properties, *J. Colloid Interface Sci.* 442 (2015) 97–102.
- [24] Q.M. Zheng, D.P. Durkin, J.E. Elenewski, Y.X. Sun, N.A. Banek, L.K. Hua, H.N. Chen, M.J. Wagner, W. Zhang, D.M. Shuai, Visible-light-responsive graphitic carbon nitride: rational design and photocatalytic applications for water treatment, *Environ. Sci. Technol.* 50 (2016) 12938–12948.
- [25] L.L. Feng, F. He, G.X. Yang, S.L. Gai, Y.L. Dai, C.X. Li, P.P. Yang, NIR—driven graphitic-phase carbon nitride nanosheets for efficient bioimaging and photodynamic therapy, *J. Mater. Chem. B* 4 (2016) 8000–8008.
- [26] S.F. Kang, L. Zhang, C.C. Yin, Y.G. Li, L.F. Cui, Y.G. Wang, Fast flash frozen synthesis of holey few-layer  $\text{g-C}_3\text{N}_4$  with high enhancement of photocatalytic reactive oxygen species evolution under visible light irradiation, *Appl. Catal. B: Environ.* 211 (2017) 266–274.
- [27] J.D. Xiao, J. Rabeh, J. Yang, Y.B. Xie, H.B. Cao, A. Bruckner, Fast electron transfer and  $(\text{OH})-\text{O}$ -center dot formation: key features for high activity in visible-light-driven ozonation with  $\text{C}_3\text{N}_4$  catalysts, *ACS Catal.* 7 (2017) 6198–6206.
- [28] D.H. Xia, W.J. Wang, R. Yin, Z.F. Jiang, T.C. An, G.Y. Li, H.J. Zhao, P.K. Wong, Enhanced photocatalytic inactivation of *Escherichia coli* by a novel Z-scheme  $\text{g-C}_3\text{N}_4/\text{m-Bi}_2\text{O}_4$  hybrid photocatalyst under visible light: the role of reactive oxygen species, *Appl. Catal. B: Environ.* 214 (2017) 23–33.
- [29] J.D. Xiao, Q.Z. Han, Y.B. Xie, J. Yang, Q.Z. Su, Y. Chen, H.B. Cao, Is  $\text{C}_3\text{N}_4$  chemically stable toward reactive oxygen species in sunlight-driven water treatment? *Environ. Sci. Technol.* 51 (2017) 13380–13387.
- [30] W.D. Oh, L.W. Lok, A. Veksha, A. Giannis, T.T. Lim, Enhanced photocatalytic degradation of bisphenol A with Ag-decorated S-doped  $\text{g-C}_3\text{N}_4$  under solar irradiation: Performance and mechanistic studies, *Chem. Eng. J.* 333 (2018) 739–749.
- [31] L.P. Yang, G.H. Dong, D.L. Jacobs, Y.H. Wang, L. Zang, C.Y. Wang, Two-channel photocatalytic production of  $\text{H}_2\text{O}_2$  over  $\text{g-C}_3\text{N}_4$  nanosheets modified with perylene imides, *J. Catal.* 352 (2017) 274–281.
- [32] S. Zhao, X. Zhao, S.X. Ouyang, Y.F. Zhu, Polyoxometalates covalently combined with graphitic carbon nitride for photocatalytic hydrogen peroxide production, *Catal. Sci. Technol.* 8 (2018) 1686–1695.
- [33] J. Wang, Z. Yang, W.Q. Yao, X.X. Gao, D.P. Tao, Defects modified in the exfoliation of  $\text{g-C}_3\text{N}_4$  nanosheets via a self-assembly process for improved hydrogen evolution performance, *Appl. Catal. B: Environ.* 238 (2018) 629–637.
- [34] L. Jing, R.X. Zhu, D.L. Phillips, J.C. Yu, Effective prevention of charge trapping in graphitic carbon nitride with nanosized red phosphorus modification for superior photo(electro)catalysis, *Adv. Funct. Mater.* 27 (2017) 1703484.
- [35] J. Xu, L.W. Zhang, R. Shi, Y.F. Zhu, Chemical exfoliation of graphitic carbon nitride for efficient heterogeneous photocatalysis, *J. Mater. Chem. A* 1 (2013) 14766–14772.
- [36] Y.Y. Kang, Y.Q. Yang, L.C. Yin, X.D. Kang, L.Z. Wang, G. Liu, H.M. Cheng, Selective breaking of hydrogen bonds of layered carbon nitride for visible light photocatalysis, *Adv. Mater.* 28 (2016) 6471–6477.
- [37] P. Niu, L.L. Zhang, G. Liu, H.M. Cheng, Graphene-like carbon nitride nanosheets for improved photocatalytic activities, *Adv. Funct. Mater.* 22 (2012) 4763–4770.
- [38] S.J. Jiang, C.B. Xiong, S.Q. Song, B. Cheng, Plasmonic graphene-like Au/ $\text{C}_3\text{N}_4$  nanosheets with barrier-free interface for photocatalytically sustainable evolution of active oxygen species, *ACS Sustain. Chem. Eng.* 7 (2019) 2018–2026, <https://doi.org/10.1021/acssuschemeng.8b04338>.
- [39] S.Q. Song, C.H. Lu, X. Wu, S.J. Jiang, C.Z. Sun, Z.G. Le, Strong base  $\text{g-C}_3\text{N}_4$  with perfect structure for photocatalytically eliminating formaldehyde under visible-light irradiation, *Appl. Catal. B: Environ.* 227 (2018) 145–152.
- [40] S.X. Min, G.X. Lu, Enhanced electron transfer from the excited Eosin Y to mpg- $\text{C}_3\text{N}_4$  for highly efficient hydrogen evolution under 550 nm irradiation, *J. Phys. Chem. C* 116 (2012) 19644–19652.
- [41] Z. Li, C. Kong, G.X. Lu, Visible photocatalytic water splitting and photocatalytic two-electron oxygen formation over Cu- and Fe-doped  $\text{g-C}_3\text{N}_4$ , *J. Phys. Chem. C* 120 (2016) 56–63.
- [42] Z. Li, Y.Q. Wu, G.X. Lu, Highly efficient hydrogen evolution over  $\text{Co}(\text{OH})_2$  nanoparticles modified  $\text{g-C}_3\text{N}_4$  co-sensitized by Eosin Y and Rose Bengal under visible light irradiation, *Appl. Catal. B: Environ.* 188 (2016) 56–64.
- [43] X. Wu, S.J. Jiang, S.Q. Song, C.Z. Sun, Constructing effective photocatalytic purification system with P-introduced  $\text{g-C}_3\text{N}_4$  for elimination of  $\text{UO}_2^{2+}$ , *Appl. Surf. Sci.* 430 (2018) 371–379.
- [44] X. Wu, C.H. Lu, J.J. Liu, S.Q. Song, C.Z. Sun, Constructing efficient solar light photocatalytic system with Ag-introduced carbon nitride for organic pollutant elimination, *Appl. Catal. B: Environ.* 217 (2017) 232–240.
- [45] W.N. Xing, G. Chen, C.M. Li, Z.H. Han, Y.D. Hu, Q.O. Meng, Doping effect of non-metal group in porous ultrathin  $\text{g-C}_3\text{N}_4$  nanosheets towards synergistically improved photocatalytic hydrogen evolution, *Nanoscale* 10 (2018) 5239–5245.
- [46] G.G. Zhang, X.C. Wang, A facile synthesis of covalent carbon nitride photocatalysts by co-polymerization of urea and phenylurea for hydrogen evolution, *J. Catal.* 307 (2013) 246–253.
- [47] Y. Jiao, Y. Zheng, P. Chen, M. Jaroniec, S.Z. Qiao, Molecular scaffolding strategy with synergistic active centers to facilitate electrocatalytic  $\text{CO}_2$  reduction to hydrocarbon/alcohol, *J. Am. Chem. Soc.* 139 (2017) 18093–18100.
- [48] W. Iqbal, B.C. Qiu, Q.H. Zhu, M.Y. Xing, J.L. Zhang, Self-modified breaking hydrogen bonds to highly crystalline graphitic carbon nitrides nanosheets for drastically enhanced hydrogen production, *Appl. Catal. B: Environ.* 232 (2018) 306–313.
- [49] A. Cohen, Y.Z. Yang, Q.L. Yan, A. Shlomovich, N. Petrutik, L. Burstein, S.P. Pang, M. Gozin, Highly thermostable and insensitive energetic hybrid coodiation polymers based on graphene oxide-Cu(II) complex, *Chem. Mater.* 28 (2016) 6118–6126.
- [50] P.F. Xia, B.C. Zhu, B. Cheng, J.G. Yu, J.S. Xu, 2D/2D  $\text{g-C}_3\text{N}_4/\text{MnO}_2$  nanocomposite as a direct Z-scheme photocatalyst for enhanced photocatalytic activity, *ACS Sustain. Chem. Eng.* 6 (2018) 965–973.
- [51] T. Zhang, D. Zhang, X.H. Han, T. Dong, X.W. Guo, C.S. Song, R. Si, W. Liu, Y.F. Liu, Z.K. Zhao, Preassembly strategy to fabricate porous hollow carbonitride spheres inlaid with single Cu-N3 sites for selective oxidation of benzene to phenol, *J. Am. Chem. Soc.* 140 (2018) 16936–16940.
- [52] Y.Y. Ni, Z.Y. Chen, F.T. Kong, Y. Qiao, A.G. Kong, Y.K. Shan, Space-confined synthesis of multilayer Cu-N-doped graphene nanosheets for efficient oxygen electroreduction, *Dalton Trans.* 46 (2017) 8586–8592.
- [53] P.F. Xia, M.J. Liu, B. Cheng, J.G. Yu, L.Y. Zhang, Dopamine modified  $\text{g-C}_3\text{N}_4$  and its enhanced visible-light photocatalytic  $\text{H}_2$ -production activity, *ACS Sustain. Chem. Eng.* 6 (2018) 8945–8953.
- [54] M. Krulk, M. Jaroniec, Gas adsorption characterization of ordered organic-inorganic nanocomposite materials, *Chem. Mater.* 13 (2001) 3169–3183.
- [55] T. Moriuchi, T. Hirao, Design and redox function of conjugated complexes with polyanilines or quinonediimines, *Acc. Chem. Res.* 45 (2012) 347–360.
- [56] N. Wang, J. Wang, J.H. Hu, X.Q. Lu, J. Sun, F. Shi, Z.H. Liu, Z.B. Lei, R.B. Jiang, Design of palladium-doped  $\text{g-C}_3\text{N}_4$  for enhanced photocatalytic activity toward hydrogen evolution reaction, *ACS Appl. Energy Mater.* 1 (2018) 2866–2873.
- [57] J.S. Zhang, M.W. Zhang, S. Liu, X.Z. Fu, X.C. Wang, Molecular doping of carbon nitride photocatalysts with tunable bandgap and enhanced activity, *J. Catal.* 310 (2014) 24–30.
- [58] S.W. Cao, Q. Huang, B.C. Zhu, J.G. Yu, Trace-level phosphorus and sodium co-doping of  $\text{g-C}_3\text{N}_4$  for enhanced photocatalytic  $\text{H}_2$  production, *J. Power Sources* 351 (2017) 151–159.
- [59] K. Das, S.N. Sharma, M. Kumar, S.K. De, Morphology dependent luminescence properties of Co doped  $\text{TiO}_2$  nanostructures, *J. Phys. Chem. C* 113 (2009) 14783–14792.
- [60] D.P. Guo, S.Q. Xiao, K. Fan, J.G. Yu, Hierarchical  $\text{TiO}_2$  submicrorods improve the photovoltaic performance of dye-sensitized solar cells, *ACS Sustain. Chem. Eng.* 5 (2017) 1315–1321.
- [61] Q.J. Xiang, J.G. Yu, M. Jaroniec, Preparation and enhanced visible-light photocatalytic  $\text{H}_2$ -production activity of graphene/ $\text{C}_3\text{N}_4$  composites, *J. Phys. Chem. C* 115 (2011) 7355–7363.
- [62] X.L. Zhang, X.X. Zhang, J.D. Li, J.H. Sun, J. Bian, J.S. Wang, Y. Qu, R. Yan, C.L. Qin, L.Q. Jing, Exceptional visible-light activities of  $\text{g-C}_3\text{N}_4$  nanosheets dependent on the unexpected synergistic effects of prolonging charge lifetime and catalyzing  $\text{H}_2$  evolution with  $\text{H}_2\text{O}_2$ , *Appl. Catal. B: Environ.* 237 (2018) 50–58.
- [63] J.S. Wang, C.L. Qin, H.J. Wang, M.N. Chu, A. Zada, X.L. Zhang, J.D. Li, F. Raziq, Y. Qu, L.Q. Jing, Exceptional photocatalytic activities for  $\text{CO}_2$  conversion on Al-O bridged  $\text{g-C}_3\text{N}_4/\alpha\text{-Fe}_2\text{O}_3$  z-scheme nanocomposites and mechanism insight with isotopes, *Appl. Catal. B: Environ.* 221 (2018) 459–466.
- [64] J.J. Kong, Z.B. Rui, H.B. Ji, Carbon nitride polymer sensitization and nitrogen doping of  $\text{SrTiO}_3/\text{TiO}_2$  nanotube heterostructure toward high visible light photocatalytic performance, *Ind. Eng. Chem. Res.* 56 (2017) 9999–10008.
- [65] W.J. Yang, Y.F. Zhu, F. You, L. Yan, Y.J. Ma, C.Y. Lu, P.Q. Gao, Q. Hao, W.L. Li, Insights into the surface-defect dependence of molecular oxygen activation over birnessite-type  $\text{MnO}_2$ , *Appl. Catal. B: Environ.* 233 (2018) 184–193.
- [66] S.J. Liu, F.T. Li, Y.L. Li, Y.J. Hao, X.J. Wang, B. Li, R.H. Liu, Fabrication of ternary  $\text{g-C}_3\text{N}_4/\text{Al}_2\text{O}_3/\text{ZnO}$  heterojunctions based on cascade electron transfer toward molecular oxygen activation, *Appl. Catal. B: Environ.* 212 (2017) 115–128.
- [67] V.L. Prasanna, R. Vijayaraghavan, Insight into the mechanism of antibacterial activity of  $\text{ZnO}$ : surface defects mediated reactive oxygen species even in the dark, *Langmuir* 31 (2015) 9155–9162.